Nonlinear Wavefield Characteristics of Seismic Translation and Rotation in Small-Strain Deformation from Moment Tensor Simulations

Wei Li [1,2], Yun Wang [1,2,*], Chang Chen[1,2], Lixia Sun[1,3]

[1] *"MWMC" group, School of Geophysics and Information Technology, China University of Geosciences, Beijing* 100083*, China*

[2] *State Key Laboratory of Geological Processes and Mineral Resources, China University of Geosciences, Beijing* 100083*, China*

[3] *Sinopec Research Institute of Petroleum Engineering Co., Ltd., Beijing* 102206*, China*

[*] Corresponding author: wangyun@mail.gyig.ac.cn.

Abstract Seismic rotational motions recorded in near-field and strong-motion observations show discrepancies with theoretical predictions derived from linear elastodynamic theory. To investigate potential nonlinear contributions, this study incorporates geometric nonlinear effects into wave propagation theory using the Green-Lagrange strain tensor. A staggered-grid finite-difference method is used to simulate six-component (translational and rotational) wavefields generated by three fundamental seismic sources: isotropic (ISO), double-couple (DC), and compensated linear vector dipole (CLVD). The results demonstrate that nonlinear effects, as a secondary source, have a universal intensity pattern adhering to the physics of wave motion. However, the excitation efficiency and modulation of wavefield attributes (such as P-wave polarization) depend strongly on source type. Simulations show that rotational

23   components exhibit higher sensitivity to nonlinear effects driven by S-waves. Reference

24   simulations of two moderate-to-strong earthquakes suggest that surface waves are the

25   primary carriers of nonlinear features.

26

27   1 Introduction

28   Seismic rotational motion is a significant part of ground shaking, particularly

29   recordable in strong-motion events (Graizer, 1991; 2010; Zhou et al., 2019). Under

30   near-field and shallow-source conditions, these rotational motions exhibit pronounced

31   characteristics (Kozak, 2009; Sun et al., 2017) and play a critical role in the seismic

32   design and stability assessment of structures (Li, 1991; Yan, 2017; Huras et al., 2021).

33   Progress in research indicates that incorporating rotational motion data, which contains

34   information on the spatial gradients of the wavefield, can improve the accuracy and

35   stability of seismic source inversion (Bernauer et al., 2014; Donner, 2016; Ichinose et

36   al., 2021; Hua and Zhang, 2022).

37   In a review of advances in rotational seismology, Lee et al. (2009) suggested that

38   the measured rotational components in strong ground motion may originate from

39   nonlinear elasticity and site effects. This suggestion is based on empirical evidence

40   from observations in Japan and Taiwan, where rotational measurements are typically

41   one to two orders of magnitude larger than those expected from classical linear

42   elasticity theory or derived from translational data, indicating the limitations of linear

43   theory. In geophysics, nonlinearity often refers to constitutive nonlinearity related to

44   material behavior, such as the hysteretic and elastoplastic responses of soils and rocks

45   under large strains (Bonilla et al., 2005; Bonilla et al., 2011; Frankel et al., 2002;

46   Régnier et al., 2018). This type of nonlinearity involves intrinsic energy dissipation and

47   plastic deformation, resulting in nonlinear site amplification in strong-motion records

48   (Régnier et al., 2018).

49   On the other hand, nonlinearity can also arise from the geometric description of

50   an object's deformation itself, known as geometric nonlinearity. Even if a material

51   adheres to Hooke's law, the mathematical relationship between strain and displacement

52   can still contain higher-order nonlinear terms. This geometric nonlinearity is significant

53   when describing seismic wave propagation in pre-stressed media (Tromp and Trampert,

54   2018). However, current research has predominantly focused on material constitutive

55   nonlinearity and its linearized approximation (Renaud et al., 2012; 2013; TenCate et al.,

56   2016; Feng et al., 2018), with a systematic investigation into the strain nonlinearity

57   introduced by the measure of deformation, and its expression in seismic wave

58   propagation, is still lacking. This neglected aspect may contribute to understanding the

59   complex rotational motions observed in the near field of strong earthquakes.

60   Therefore, this study aims to systematically characterize geometric nonlinear

61   effects within the framework of the small-strain assumption by incorporating the Green-

62   Lagrange strain tensor. We employ a staggered-grid finite-difference method to

63   simulate three fundamental moment tensor sources, exploring how geometric

64   nonlinearity leads to body-wave coupling and energy redistribution, and its intrinsic

65   dependence on the source type. Furthermore, using two moderate-to-strong earthquakes

66   in the Taiwan region as examples, we explore the manifestation of nonlinear effects in

67   a more complex scenario.

68   2 Theory and method

69   2.1 Elastodynamic theory

70   Consider a three-dimensional (3D) elastic medium in an orthogonal Cartesian

71   coordinate system (Fig. 1). An infinitesimal line element connecting a particle A at

72   position **x** and an adjacent particle B at **x**+d**x** has an initial length of ds. When subjected

73   to external force, this element undergoes a displacement ***u***(***x***, t), moving to new

74   positions A' and B' at **x**' and **x**'+d**x**', respectively, with a deformed length of ds'. This

75   process includes both rigid-body displacement and strain-induced distortion. The strain

76   energy density can be characterized by the quadratic form of the change in the element's

77   length, as shown in Eq. (1).

78
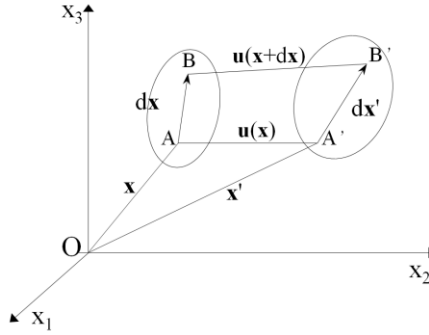
79   **Figure 1.** Schematic diagram of displacement and deformation of an infinitesimal line

80   element in an elastic medium (adapted from Aki and Richards (2002))

$$(ds')^2 - (ds)^2 = 2E_{ij}dx_i dx_j, \ i,j \in \{1,2,3\} \tag{1}$$

82   where E_{ij} is the Green-Lagrange strain tensor, which provides an objective measure of

83   deformation. In Cartesian coordinates, E_{ij} is defined by the displacement field as:

$$E_{ij} = \frac{1}{2}\left(\frac{\partial u_j}{\partial x_i} + \frac{\partial u_i}{\partial x_j} + \frac{\partial u_k}{\partial x_i} \cdot \frac{\partial u_k}{\partial x_j}\right), \ i,j,k \in \{1,2,3\} \tag{2}$$

85   The displacement gradient tensor can be decomposed into a symmetric strain tensor

86   (e_{ij}) and an antisymmetric rotation tensor (r_{ij}):

$$\frac{\partial u_j}{\partial x_i} = e_{ij} + r_{ij} \tag{3}$$

88   where,

89
$$e_{ij} = \frac{1}{2}(\frac{\partial u_j}{\partial x_i} + \frac{\partial u_i}{\partial x_j}), \quad r_{ij} = \frac{1}{2}(\frac{\partial u_i}{\partial x_j} - \frac{\partial u_j}{\partial x_i}) \tag{4}$$

90   Traditional linear elasticity simplifies the problem by neglecting the second-order

91   product of displacement gradients in Eq. (2), thus reducing the Green-Lagrange strain

92   tensor to the strain tensor e_{ij}:

93
$$E_{ij} \approx e_{ij} = \frac{1}{2}(\frac{\partial u_j}{\partial x_i} + \frac{\partial u_i}{\partial x_j}) \tag{5}$$

94   For an isotropic medium, the stress-strain constitutive relationship is linear

95   (generalized Hooke's law), given by Eq. (6), where λ and μ are the Lamé constants.

96
$$\sigma_{ij} = \lambda \delta_{ij} e_{kk} + 2\mu e_{ij} \tag{6}$$

97   The theoretical framework of this study consistently employs the linear

98   constitutive relationship described by Eq. (6). However, the complete Green-Lagrange

99   strain tensor E_{ij} (rather than its linear approximation e_{ij}) is substituted into it, yielding a

100   stress expression that reflects geometric nonlinearity:

101
$$\sigma_{ij} = \lambda \delta_{ij} e_{kk} + 2\mu e_{ij} + \underbrace{\frac{1}{2}\lambda \delta_{ij}(\frac{\partial u_k}{\partial x_m} \cdot \frac{\partial u_k}{\partial x_m}) + \mu \frac{\partial u_k}{\partial x_i} \cdot \frac{\partial u_k}{\partial x_j}}_{\text{additional terms}}, \quad i,j,k,m \in \{1,2,3\} \tag{7}$$

102   Substituting this stress expression into the momentum conservation law (Eq. (8)),

103
$$\rho \frac{\partial^2 u_i}{\partial t^2} = \frac{\partial \sigma_{ij}}{\partial x_j} \tag{8}$$

104   where ρ is the medium density, we finally obtain the nonlinear wave equation:

105
$$\rho \frac{\partial^2 u_i}{\partial t^2} = \underbrace{(\lambda+\mu)\frac{\partial^2 u_j}{\partial x_i \partial x_j} + \mu \frac{\partial^2 u_i}{\partial x_j \partial x_j}}_{\text{original terms}} + \underbrace{\lambda \frac{\partial u_k}{\partial x_i}\frac{\partial^2 u_k}{\partial x_j x_j} + \mu\left(\frac{\partial^2 u_k}{\partial x_i x_j}\cdot\frac{\partial u_k}{\partial x_j} + \frac{\partial^2 u_k}{\partial x_j x_j}\cdot\frac{\partial u_k}{\partial x_i}\right)}_{\text{additional terms}}, \quad i,j,k \in \{1,2,3\} \tag{9}$$

106   In Eq. (9), under the small-strain assumption, the original terms constitute the

107   classic wave equation, while the subsequent additional terms arise from the geometric

108   nonlinearity of strain. These additional terms mathematically act as endogenous,

109   secondary body force sources that depend on the wavefield itself. In linear theory, P-

110   waves (driven by the divergence field, representing volume change) and S-waves

111   (driven by the curl field, representing shape change) are strictly decoupled. However,

112   the existence of these nonlinear terms disrupts this decoupling. Specifically, the term

113    $\partial u_k / \partial x_i \cdot \partial u_k / \partial x_j$ is a product of displacement gradients (which include both strain and

114   rotation). When the P-wave (dominated by compressional strain) propagates, its non-

115   uniform strain field generates spatial gradients. Through these higher-order terms, the

116   gradient field of the P-wave can generate an equivalent body force source with a curl

117   component within the medium, which in turn radiates S-waves. The reverse is also true.

118   This is the fundamental physical mechanism of P-S mode conversion: energy is

119   transferred between the compressional and shear modes through the self-interaction of

120   the wavefield.

121   2.2 Staggered-grid finite-difference method

122   To solve the nonlinear wave equation (9), we employ a high-accuracy Staggered-

123   Grid Finite-Difference (SGFD) method (Virieux, 1986; Sun et al., 2018). First, by

124   taking the time derivative of the nonlinear constitutive relation (7) and combining it

125   with the momentum conservation equation (8), we convert the second-order wave

126   equation into a system of first-order velocity-stress partial differential equations. This

127   system includes additional stress-rate terms generated by the second-order products of

128   displacement gradients. These terms update the displacement field through time

129　integration of the velocity field, thereby implementing the nonlinear coupling. The

130　resulting velocity-stress equations are:

131
$$
\begin{cases}
\rho \dfrac{\partial v_i}{\partial t} = \dfrac{\partial \sigma_{ij}}{\partial x_j} \\[2mm]
\dfrac{\partial \sigma_{ij}}{\partial t} = \lambda \delta_{ij} \dfrac{\partial E_{kk}}{\partial t} + 2\mu \dfrac{\partial E_{ij}}{\partial t} \\[2mm]
\quad = \lambda \delta_{ij} \dfrac{\partial v_k}{\partial x_k} + \mu\left(\dfrac{\partial v_i}{\partial x_j} + \dfrac{\partial v_j}{\partial x_i}\right) + \underbrace{\lambda \delta_{ij}\left(\dfrac{\partial v_k}{\partial x_m}\cdot\dfrac{\partial u_k}{\partial x_m}\right) + 2\mu \dfrac{\partial v_k}{\partial x_i}\cdot\dfrac{\partial u_k}{\partial x_j}}_{\text{additional terms}}
\end{cases}
, \; i,j,k,m \in \{x,y,z\} \quad (10)
$$

132　　　where $v_i = \partial u_i / \partial t$. In the SGFD scheme, different physical quantities are staggered

133　on the spatial grid cells. This arrangement naturally satisfies the central-difference

134　approximation for differential operators, effectively suppressing numerical dispersion

135　and enhancing computational stability and accuracy, as illustrated in Fig. 2.

136
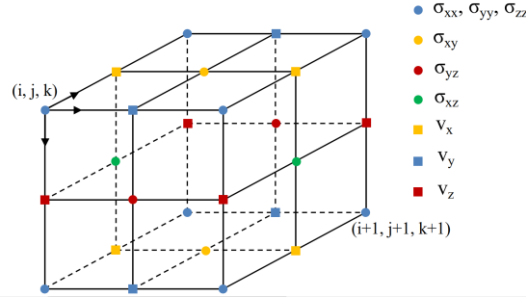
137　　　**Figure 2.** 3D staggered-grid configuration for velocity-stress formulations,

138　　　showing the placement of velocity componentsand stress components.

139　　　To handle the model's truncated boundaries, we employ the Perfectly Matched

140　Layer (PML) absorbing boundary condition (Li et al., 2015). For simulations involving

141　a free surface, the free boundary is implemented at the top of the model by setting the

142　acoustic boundary replacement (Xu et al., 2007; Wang et al., 2012). The numerical code

143　used in this study has been benchmarked against international standard programs,

144　including SPICE/SISMOWINE and SPECFEM2D. The comparison is provided in the

145   supplementary material.

146   2.3 Source implementation and simulation parameters

147   The seismic moment tensor M_{ij} is the complete representation of an equivalent

148   body-force system for a point source (Gilbert, 1970). It can be decomposed into three

149   fundamental components: isotropy (ISO), double couple (DC), and compensated linear

150   vector dipole (CLVD) (Knopoff and Randall, 1970; Jost and Hermann, 1989). These

151   moment tensor expressions can be written as Eq. (11).

$$
\boldsymbol{M}^{ISO} = \begin{pmatrix} M_{xx} & 0 & 0 \\ 0 & M_{yy} & 0 \\ 0 & 0 & M_{zz} \end{pmatrix}, \boldsymbol{M}^{DC} = \begin{pmatrix} 0 & M_{xy} & 0 \\ M_{yx} & 0 & 0 \\ 0 & 0 & 0 \end{pmatrix}, \boldsymbol{M}^{CLVD} = \begin{pmatrix} M_{xx} & 0 & 0 \\ 0 & M_{yy} & 0 \\ 0 & 0 & -2M_{zz} \end{pmatrix} \tag{11}
$$

152

153   In our SGFD framework, we follow the method proposed by Graves (1996) to

154   implement the moment tensor source by converting the moment rate tensor into

155   equivalent body forces. The equivalent velocity increment Δv^n added on the grid can

156   be expressed as:

$$
\boldsymbol{M}^{ISO} : \Delta v_i^n = \frac{M_{ij} \cdot dt \cdot f^n}{\rho V} \cdot \frac{\partial}{\partial x_j}
$$

157
$$
\boldsymbol{M}^{DC} : \Delta v_i^n = \frac{M_{jk} \cdot dt \cdot f^n}{\rho V} \cdot (\delta_{ij} \frac{\partial}{\partial x_k} + \delta_{ik} \frac{\partial}{\partial x_j}) \tag{12}
$$

$$
\boldsymbol{M}^{CLVD} : \Delta v_i^n = \frac{M_{kl} \cdot dt \cdot f^n}{\rho V} \cdot (\delta_{ik} \frac{\partial}{\partial x_l} + \delta_{il} \frac{\partial}{\partial x_k} - \frac{2}{3} \delta_{kl} \frac{\partial}{\partial x_i})
$$

158   where $i, j, k, l \in \{x, y, z\}$. Δv is the velocity increment, n is the time-step index, dt is the

159   time step, ρ is the density, V is the grid cell volume, and f^n is the value of the source-

160   time function at time n·dt.

161   We conduct simulations in a homogeneous, isotropic, 3D full-space model to

162   isolate the effects of nonlinearity from those of complex media. The model parameters

163   are: P-wave velocity v_p=4400 m/s, S-wave velocity v_s=3000 m/s, and density ρ=2600

164 kg/m^3. The model space is 14 km × 14 km ×14 km, with a uniform grid spacing of Δx

165 = Δy = Δz = 50 m. The source is located at the model center. It uses a Ricker wavelet

166 with a dominant frequency of 4 Hz as the source-time function. Receivers are arranged

167 on a spherical surface with a radius of 5 km centered at the source to sample wavefields

168 at various azimuths. The time step is Δt = 0.0015s.

169   The shortest wavelength for the 4 Hz dominant frequency is the S-wavelength (λ_S

170 = 750 m). Based on the 50 m grid spacing, there are 15 grid points per wavelength,

171 which is well above the threshold required for high-order finite-difference schemes

172 (Virieux, 1986). The Courant-Friedrichs-Lewy (CFL) number is approximately 0.23,

173 which is well below the stability limit for 3D finite-difference methods (Moczo et al.,

174 2007), ensuring the stability and accuracy of the numerical computation.

175 3 Comparison of simulation results

176 3.1 Basic characteristics of nonlinear seismic wavefields

177   Fig. 3(a) displays the 6C wavefield snapshots for the ISO source at t=1.5s, while

178 Fig. 3(b) compares the linear and nonlinear waveforms recorded at a specific receiver.

179 Within the framework of linear theory, an ISO source only generates P-waves in

180 homogeneous elastic media. However, a faint signal is still recorded in the P-wave

181 window of the rotational components in the linear simulation (black line). This signal

182 originates from the spatial gradients produced by the wavefront curvature of the near-

183 field P-wave. In the far field, P-wavea can be approximated as an irrotational plane

184 wave with no curl in its displacement field. In the near field, however, the spatial

185   gradients of its displacement field can generate weak rotation. This signal is very weak

186   compared to the rotational signals generated by S-waves, and is therefore treated in this

187   study as the baseline background for assessing the nonlinear contributions.

188   The waveform comparison shows that in the S-wave window, the nonlinear

189   simulation exhibits a distinct response with obvious amplitude, whereas the linear

190   simulation is near zero in the ISO results. This vibration is attributed to the P-to-S mode

191   conversion of energy, caused by geometric nonlinearity. Analysis of the waveform

192   characteristics in Fig. 3(b) reveals that the EM caused by nonlinearity is larger in the

193   rotational components than in the translational ones, while the PM is nearly zero. This

194   indicates that the primary effect of geometric nonlinearity is to modulate the energy

195   distribution and envelope shape of the waves, rather than perturbing their propagation

196   velocity or arrival time. This effect originates from the higher-order nonlinear terms in

197   the strain-displacement relationship. These terms act as new, endogenous body force

198   terms in the wave equation, equivalent to producing minor secondary perturbations in

199   the wave's propagation. These perturbations interact with the primary wavefield,

200   thereby reallocating energy and ultimately altering the wave's amplitude and shape. For

201   instance, as a P-wave from an ISO source propagates, its non-uniform strain field

202   generates spatial gradients. Through the self-interaction of these gradients via the

203   nonlinear terms, an equivalent body force source with a curl component is generated

204   within the medium, which then radiates S-waves.
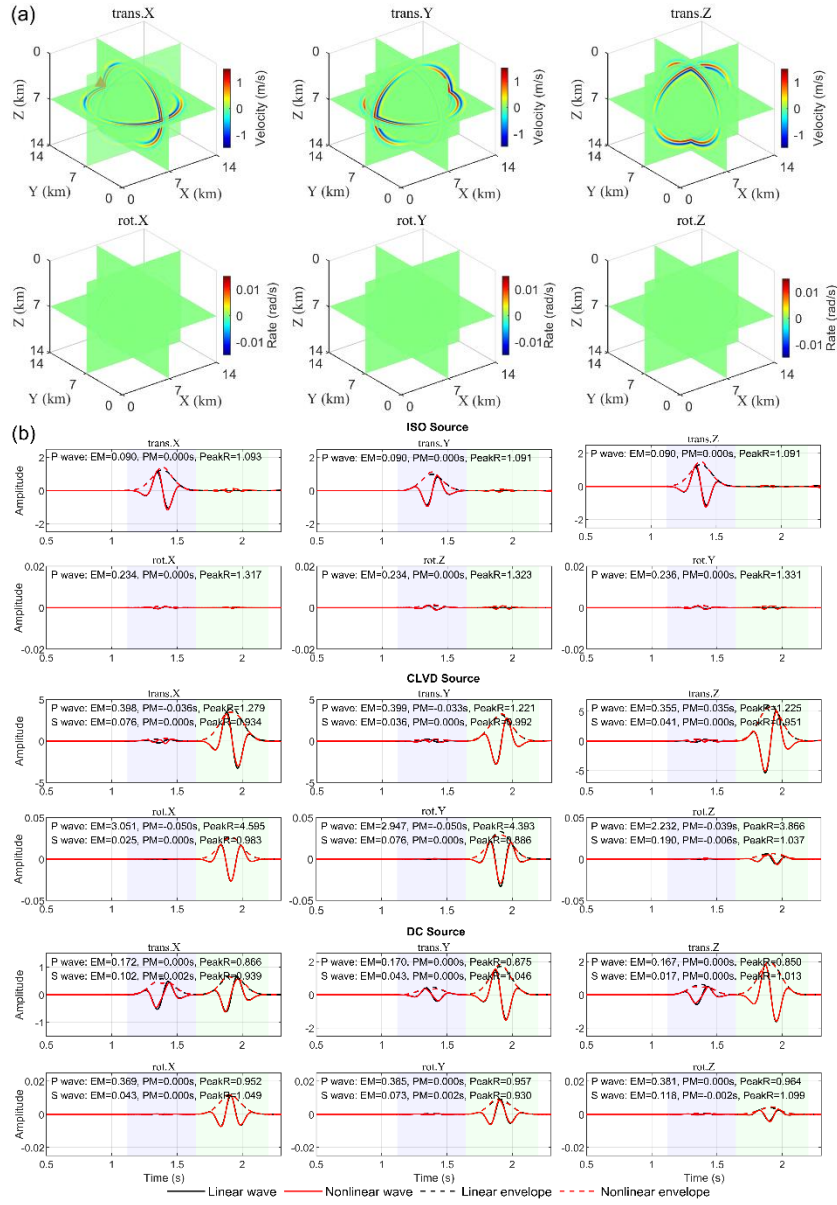
Figure 3. (a) Snapshot of the 6C wavefield from the linear ISO source simulation and

the location of the example receiver (indicated by the red triangle on the trans.X

component). (b) Comparison of the waveforms and envelope characteristics of the

linear and nonlinear simulations at this receiver. The P-wave and S-wave analysis

windows are marked. EM: envelope misfit; PM: phase misfit; PeakR: Peak ratio.

We next calculated the energy of the residual waveforms between the linear and

nonlinear simulations. Fig. 4 shows the projection of this metric in the P-wave and S-

215   wave windows onto three principal planes.

216

217
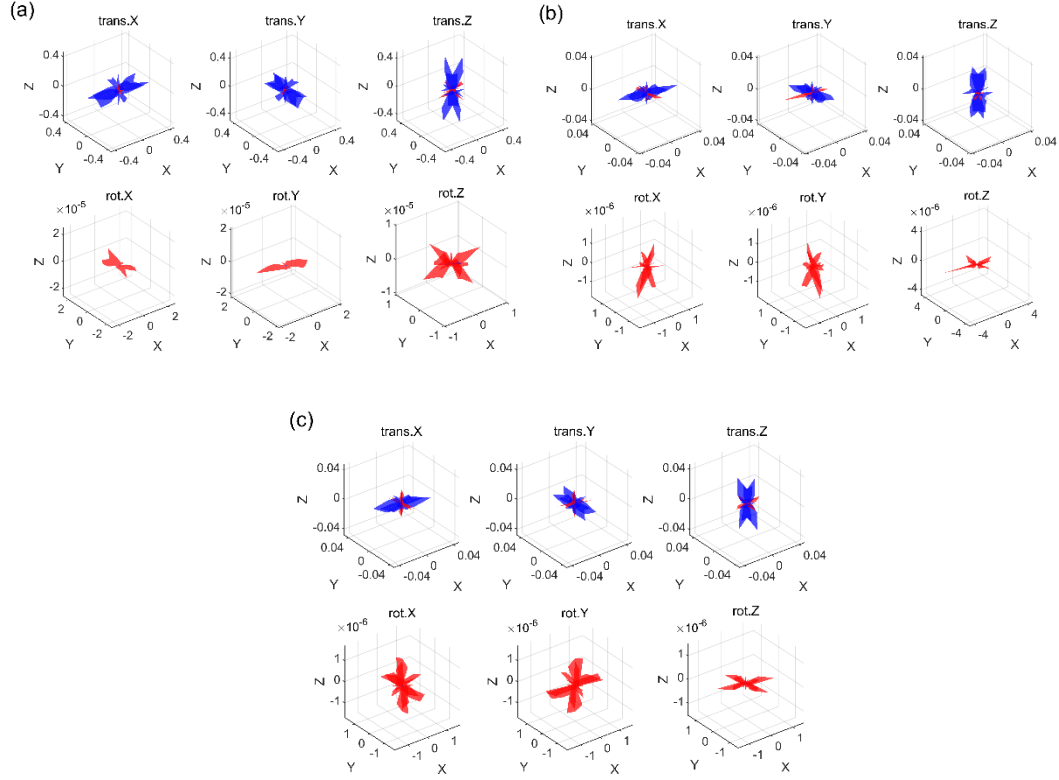
**Figure 4.** 3D spatial projection of the intensity of waveform perturbations

generated by nonlinearity. (a)-(c) are the results for CLVD, DC, and ISO sources,

respectively. Each subplot shows the projection of the nonlinear effect intensity of the

P-wave (blue) and the S-wave (red).

    The results indicate that the radiation of the nonlinear effect follows fundamental

wave physics principles. In the translational components, the nonlinear effect of the P-

wave is much stronger than that of the S-wave, and its dominant direction is consistent

with the corresponding coordinate axes, reflecting the direction of the strongest strain

gradient in the linear P-wave field. Consequently, the nonlinear effect is strongest in the

direction where the theoretical linear P-wave amplitude projects most strongly onto the

corresponding Cartesian component (e.g., the X-axis direction for the trans.X

229   component). In the rotational components, the nonlinear perturbation in the S-wave is

230   dominant. This is because rotational motion is generated by shear strain gradients, and

231   the S-wave, carrying substantial shear energy, is most effective at producing the shear

232   strain gradients required to drive rotation.

233   Building on the time-domain analysis, spectral analysis was conducted on

234   waveforms in the P- and S-wave windows of the median and interquartile range (IQR)

235   of the Power Spectral Density (PSD), as shown in Fig. 5. For the CLVD and DC sources,

236   the median nonlinear spectrum is systematically higher than the median linear spectrum

237   in the mid-to-high frequency band (approx. 5-20 Hz) in both P- and S-waves, and this

238   phenomenon is more pronounced in the rotational components. The translational

239   component spectra are nearly identical in the ISO source simulation. In the S-wave

240   comparison for the ISO source, the linear translational and rotational energies are

241   extremely low, essentially at the level of numerical simulation noise. In contrast, the

242   nonlinear spectrum is several orders of magnitude higher, providing frequency-domain

243   evidence for the nonlinear P-S mode conversion. The IQR of the PSD indicates that the

244   nonlinear effects exhibit strong spatial variability, being enhanced in some azimuths

245   while potentially being weakened in others, thus showing significant azimuthal

246   dependence. The spectral comparison reveals a key feature of the nonlinear effect:

247   energy transfer to higher frequencies. The energy injected by the source, primarily

248   concentrated at lower frequencies, is efficiently pumped by the nonlinear secondary

249   source and re-radiated as higher-frequency energy. This redistribution of high-

250   frequency energy, accompanied by the mode conversion of P- and S-waves, collectively

251 causes the nonlinear spectral lines to be systematically higher than the linear ones in

252 the mid-to-high frequency range.
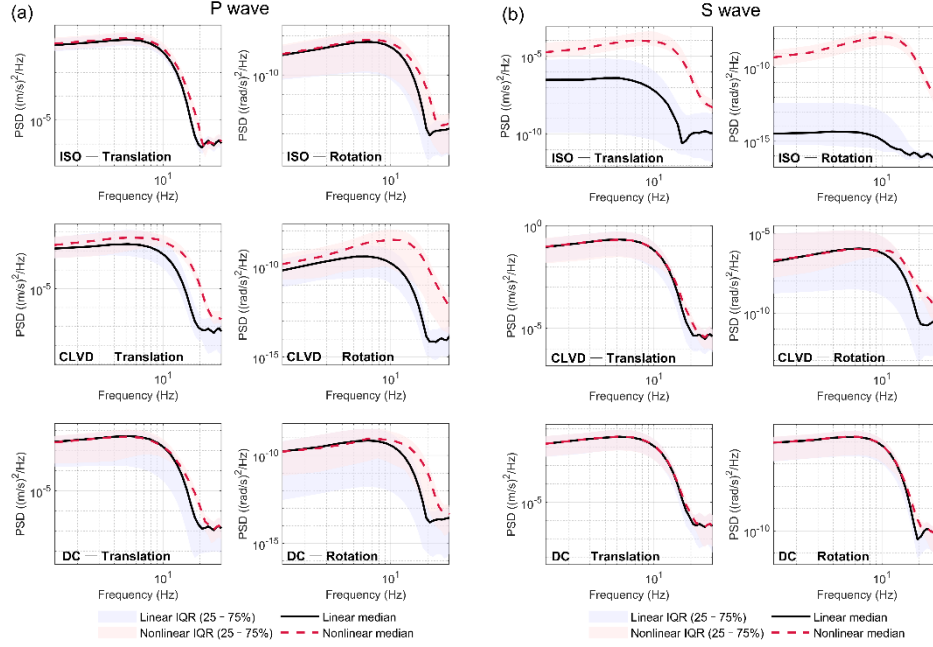
**Figure 5.** Comparison of the (a) P-wave and (b) S-wave PSD of translational and rotational components. The black solid line is the median PSD from the linear simulations, the red dashed line is from the nonlinear simulations, and the shaded area represents the 25%-75% IQR.

3.1 Source-type dependency of nonlinear effects

259 Fig. 6 presents the log-ratio of nonlinear to linear energy ($\log(E_{nl} / E_{lin})$) for the

260 tangential energy in the P-wave (E^P) and the radial energy in the S-wave (E^S). The

261 energy E is obtained by time-integrating the square of the wavefield amplitude. Fig. 6,

262 through scatter plots and statistics, shows the distribution of the logarithmic energy

263 ratios for the three source types, quantitatively assessing the overall impact of nonlinear

264 effects on the energy of specific wave types.

265 Regarding the tangential energy in the P-wave (Fig. 6(a)), the nonlinear

266 enhancement is most significant for the CLVD source, followed by the DC source,

267 while the effect of the ISO source is minimal. This indicates that the CLVD source is

268 the most effective mechanism for exciting the nonlinear growth of P-wave tangential

269 energy. For the radial energy in the S-wave (Fig. 6(b)), the net effect of nonlinearity for

270 the CLVD and DC sources is not statistically significant, possibly due to the

271 cancellation of azimuthal enhancement and reduction.

272
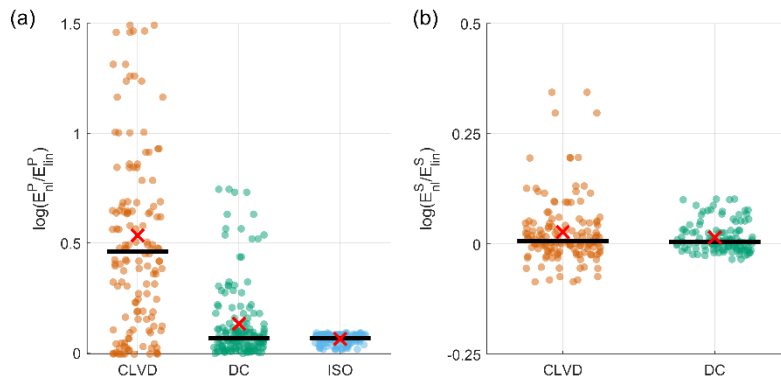
273 **Figure 6.** Distribution of the nonlinear/linear log-ratio for (a) tangential energy

274 in the P-wave and (b) radial energy in the S-wave. The dots represent the values for

275 each independent receiver; the black bar indicates the median of the data; the red

276 cross indicates the arithmetic mean.

277 To further investigate the impact of nonlinearity on the micro-properties of the

278 wavefield, we introduce two quantitative metrics to analyze the waveform attribute

279 changes within the P-wave window. First, we use rectilinearity (rect) to measure the

280 deviation of P-wave particle motion from a straight line. This metric is calculated based

281 on the eigenvalues of the covariance matrix. The sign of the change, $\Delta\text{rect} = \text{rect}_{nl}$ -

282 rect_{lin}, reflects whether the nonlinearity promotes or suppresses the leakage of P-wave

283 energy into the tangential direction. Second, to explore the coupling relationship

284   between different motion modes, we introduce the rotation-translation correlation (corr).

285   This metric calculates the Spearman's rank correlation coefficient between the time

286   series of the tangential velocity magnitude and the rotation rate magnitude, quantifying

287   the synchrony of the time-varying intensity envelopes of these two physical motions.

288   Fig. 7(a) shows the statistical distribution of the differences in these two metrics.

289   For all three sources, Δcorr is generally positive, indicating that geometric nonlinearity

290   may be a common physical mechanism that enhances the coupling between rotation

291   and translation. In contrast, the distribution of Δrect shows a pronounced source

292   dependence: the ISO source causes weak changes, the DC source induces significant

293   negative changes, while the CLVD source primarily causes positive changes. The

294   spatial distribution of Δrect in Fig. 7(b) further reveals its essential connection to the

295   source's strain state. For the ISO source, characterized by pure volumetric strain, the

296   pure volumetric strain excites a very weak shear effect through nonlinearity, leading to

297   a slight decrease in P-wave rectilinearity, but the efficiency of this conversion is

298   extremely low. For the pure-shear DC source, the significant decrease in rectilinearity

299   is concentrated near the P-wave radiation nodes, which are the regions with the

300   strongest linear shear strain gradients. This indicates that in these regions, the efficiency

301   of the nonlinear P-S mode conversion is highest, leading to a noticeable decrease in

302   rectilinearity. For the CLVD source, which combines strong uniaxial compression and

303   axisymmetric shear, the increase in rectilinearity is also concentrated in regions with

304   strong strain gradients. The result reveals that, in a complex stress state with coexisting

305   tension and compression, the nonlinear effect may instead constrain energy to propagate

306   in the radial direction, suppressing leakage into the tangential direction, thereby

307   purifying the P-wave motion.
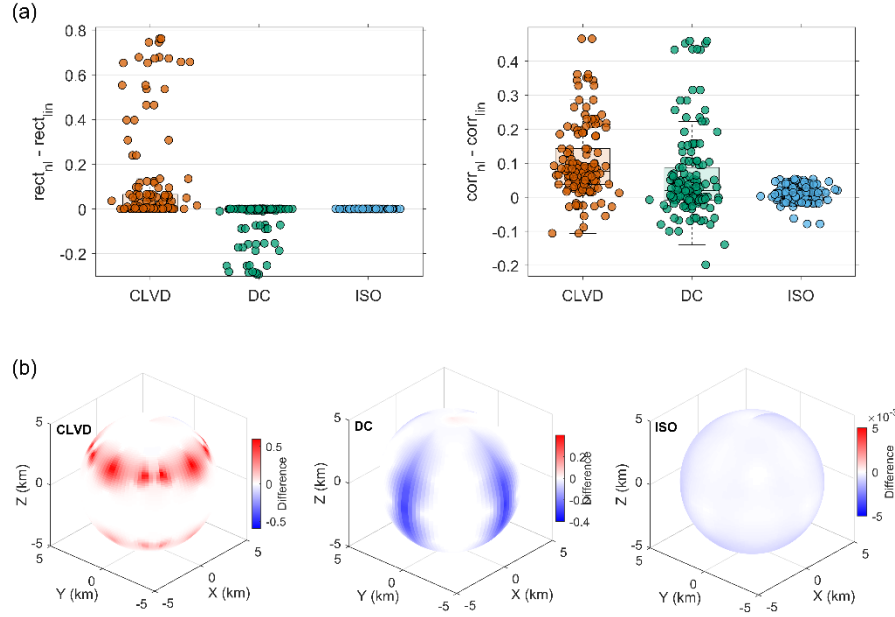
Figure 7. (a) Statistical distribution of the change in P-wave rectilinearity and

rotation-translation correlation changes, and (b) spherical spatial distribution of Δrect

in different receivers.

In summary, the analysis of the wavefield properties demonstrates that the

manifestation of nonlinear effects is fundamentally controlled by the type of strain field

initialized by the source and the geometry of its spatial gradients. Different source

mechanisms, by initializing different strain fields, thus modulate the mode, intensity,

and even the effect of the nonlinear response.

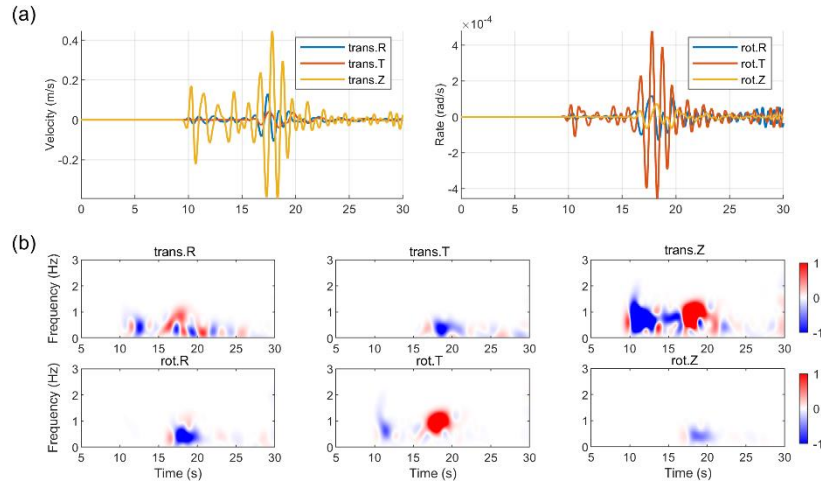## 4 Simulation of nonlinear effects for referenced earthquake events

To extend the understanding established in the idealized full-space model to more

realistic scenarios involving complex propagation effects, we further simulate two

moderate-to-strong referenced earthquakes that occurred in the coastal region of

322   Taiwan: event E1 (Mw 5.4) and event E2 (Mw6.1). The epicenters and station locations

323   of these two referenced events are shown in Fig. S4. Unlike the preceding basic source

324   simulations, the models in this section employ a layered velocity structure based on the

325   CRUST1.0 model (Laske et al., 2013) to approximate the real Earth's structure (see

326   Table S5). The source mechanisms for both events (Eq. (13)) are mixed sources. Other

327   detailed simulation parameters for the two referenced earthquake simulations are

328   provided in Table S6.

329
$$E1: \begin{bmatrix} M_{xx} = -7.569 \times 10^{16}, M_{yy} = -2.373 \times 10^{16}, M_{zz} = 9.942 \times 10^{16} \\ M_{xz} = 7.372 \times 10^{16}, M_{yz} = -1.0965 \times 10^{17}, M_{xy} = 4.156 \times 10^{16} \end{bmatrix}$$
$$E2: \begin{bmatrix} M_{xx} = -1.064 \times 10^{18}, M_{yy} = -7.607 \times 10^{17}, M_{zz} = 1.8247 \times 10^{18} \\ M_{xz} = 3.141 \times 10^{17}, M_{yz} = 3.155 \times 10^{17}, M_{xy} = 1.114 \times 10^{18} \end{bmatrix}$$
(13)

330   Fig. 8 shows the results for the E1. Compare the waveforms and the time-

331   frequency energy difference in Fig. 8(b). In the translational components, the energy

332   changes induced by nonlinearity are relatively dispersed in different types of waves.

333   However, most are concentrated during the arrival of S-wave (approx. 15-20 s) and the

334   subsequent surface waves, and faint but persistent nonlinear perturbations are also

335   observed during the P-wave and its subsequent multiple reflections/conversions

336   (approx. 5-15 s). In the rotational components, the nonlinear response energy is more

337   concentrated than in the translational components. Energy perturbations can be

338   observed on the rot.T component before the direct S-wave arrival, which may

339   correspond to nonlinear effects excited by S-waves converted from P-waves or S-waves

340   reflected/transmitted within the layered medium. For the rot.R and rot.Z components,

341   the nonlinear effects are primarily associated with the arrival of the direct S-wave.

342   Different components showing different extents of nonlinearity may stem from the

343   azimuthal location of this receiver.

344

345   **Figure 8**. (a) Synthetic linear 6C waveforms and (b) normalized time-frequency

346   energy differences (the nonlinear minus the linear) for event E1.

347   Numerical simulations of the E2 (Fig.9) also show nonlinear effects. Combining

348   the time-domain waveforms (Fig. 9(a)) and the time-frequency energy difference plots

349   (Fig. 9(b)), it can be seen that significant energy changes occur in all components during

350   the arrival of the direct S-wave (approx. 90 s) and the strong surface waves. A long-

351   duration, very-low-frequency (<0.2 Hz) energy enhancement band appears in the

352   translational components, starting from the surface waves and continuing. This may

353   correspond to long-period perturbations induced by strong surface waves through

354   nonlinear mechanisms, potentially involving P-S coupling in layered media, while the

355   rotational components, as displacement gradients, are not sensitive to it.
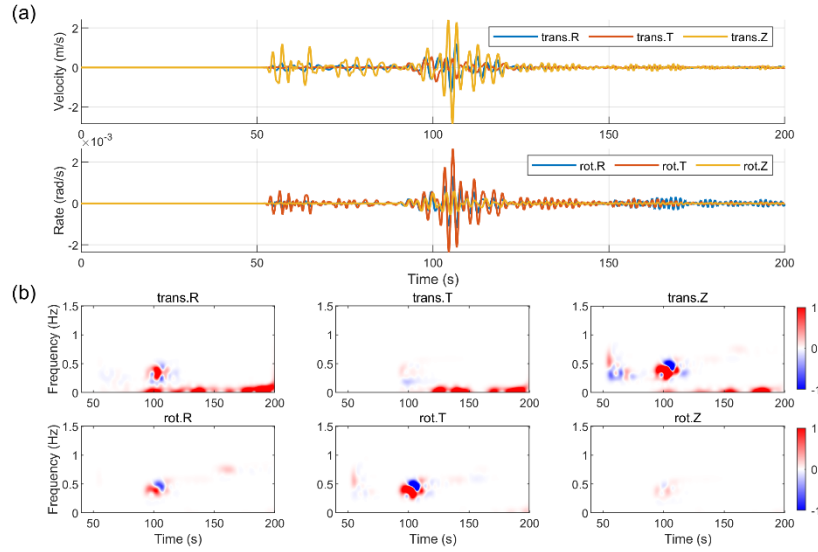
Figure 9. (a) Synthetic linear 6C waveforms and (b) normalized time-frequency

energy differences (the nonlinear minus the linear) for event E2.

By comparing the simulations of the two events, we find that the surface waves

are the primary phases that accumulate and carry nonlinear information. At the same

time, the E2 event, with its different source mechanism and further propagation path,

exhibits a long-period perturbation not seen in the E1 simulation. This suggests that in

more realistic scenarios, the physical mechanisms of nonlinear effects may be more

complex and can be influenced by many factors. The different nonlinear characteristics

displayed by the two event simulations may also be influenced by the combined effects

of their complex, mixed source mechanisms and the specific source-station azimuth.

5 Discussion

This study, through systematic simulations of fundamental seismic sources and

referenced earthquake events, has demonstrated several characteristics of geometric

nonlinearity in seismic wavefields. First, it demonstrates that the excitation and

manifestation of nonlinear effects are controlled by the strain state of the linear

372   wavefield and its spatial gradients. As predicted by nonlinear elastodynamic theory,

373   geometric nonlinearity acts as an equivalent secondary source term in the wave

374   equation, with its strength being proportional to the quadratic terms of the linear strain

375   field. The radiation of nonlinear effects strictly follows the physical nature of

376   longitudinal and transverse waves. For instance, the nonlinear perturbation generated

377   by the strain gradients of a linear P-wave radiates most strongly along the principal

378   direction of the P-wave, whereas the nonlinear rotational effect generated by the shear-

379   strain gradients of an S-wave is most pronounced in regions of maximum S-wave

380   energy. In addition, different source mechanisms (volumetric, pure shear, axisymmetric

381   shear) modulate the mode, strength, and even the effect of the nonlinear response by

382   initializing different geometries of the strain field.

383   Second, rotational motion is a sensitive indicator for detecting near-field nonlinear

384   effects driven by S-waves. This stems from the physical nature of rotation—it is the

385   spatial gradient of the displacement field and is therefore more sensitive to the

386   secondary source terms driven by strain gradients. This suggests that the deployment

387   and analysis of six-component seismic data are of irreplaceable value for identifying

388   and quantifying nonlinear geophysical processes in future observational studies.

389   Finally, the simulations of referenced earthquake events show that surface waves,

390   which are more concentrated in energy and have longer propagation paths, are the

391   primary carriers for accumulating and preserving nonlinear information, thus pointing

392   to a key focus for future observational data analysis. More importantly, in the stronger

393   E2 event, we observed a long-period perturbation not seen in the idealized models. This

394 phenomenon suggests that under realistic strong ground motion conditions, the physical

395 mechanisms of nonlinear effects may be more complex and diverse, potentially

396 involving deeper physical processes such as stress-induced anisotropy. Limitations of

397 this study, such as the use of idealized models, highlight the need for validation with

398 real seismic records. These indicate a direction for future research: how to reliably

399 separate and identify these unique nonlinear signals from collected real seismic records,

400 which is a mixture of complex source effects, 3D heterogeneous propagation effects,

401 and local site responses.

402 ## 6 Conclusions

403 By incorporating geometric nonlinearity based on the Green-Lagrange strain tensor,

404 this study has conducted 6C seismic wavefield simulations for three fundamental

405 moment tensor sources and two referenced moderate-to-strong earthquakes. The

406 research aims to investigate the characteristics of near-field nonlinear effects and their

407 dependence on source mechanisms. The main conclusions are as follows:

408 (i) Universal radiation pattern of the nonlinear secondary source and source-

409 dependent excitation efficiency. On one hand, the radiation pattern of nonlinearity is

410 universal, strictly adhering to the physics of wave motion: the nonlinear perturbation

411 generated by P-wave strain gradients radiates primarily along the axial direction (a

412 longitudinal characteristic), while the perturbation from S-wave shear-strain gradients

413 radiates mainly in the orthogonal plane directions (a transverse characteristic). This

414 pattern is independent of the initial force source type. On the other hand, the overall

415 efficiency of exciting these nonlinear secondary sources exhibits a strong source-type

dependency. Simulation results show that sources with significant shear components, such as CLVD and DC sources, are far more efficient in exciting nonlinear effects than the purely volumetric ISO source.

(ii) High sensitivity of rotational motion to S-wave-driven nonlinearity. This is primarily because rotational motion directly responds to shear-strain gradients, and S-waves are the primary carriers of shear energy. Consequently, rotational motion becomes an ideal window for detecting the secondary sources excited by S-waves, with its nonlinear response being more pronounced than that of translational components.

(iii) Effects of wave type and strain level. The strength of nonlinear effects is correlated with the strain level (which can be approximately related to the moment magnitude). More importantly, surface waves, which have more concentrated energy and longer propagation paths, are more effective carriers of nonlinear information than body waves. In the strong-motion event simulation, long-period perturbations, possibly induced by nonlinearity, were also observed. This may correspond to long-period perturbations induced by strong surface waves through nonlinear mechanisms, potentially involving P-S coupling in layered media.

Author contributions. WL: conceptualization, methodology, investigation, formal analysis, writing - original draft. YW: conceptualization, writing - original draft and revised draft. CC: investigation, formal analysis. LS: methodology.

Data availability. All data is simulated and available upon reasonable request.

438

441

Disclaimer. Publisher's note: Copernicus Publications remains neutral with regard to jurisdictional claims made in the text, published maps, institutional affiliations, or any other geographical representation in this paper.

445

448

References

Aki, K., and P. G. Richards. Quantitative seismology, 2nd ed, California: University Science Books, https://doi.org/10.1029/2003EO210008, 2002.

Bernauer, M., Fichtner, A., and Igel, H.: Reducing nonuniqueness in finite source inversion using rotational ground motions, J. Geophys. Res.-Solid Earth, 119(6), 4860-4875, https://doi.org/10.1002/2014JB011042, 2014.

Bonilla, L. F., Archuleta, R. J., and Lavallée, D.: Hysteretic and dilatant behavior of cohesionless soils and their effects on nonlinear site response: Field data observations and modeling. Bull. Seismol. Soc. Am., 95(6), 2373-2395. https://doi.org/10.1785/0120040138, 2005.

Bonilla, L. F., Tsuda, K., Pulido, N., Régnier, J., and Laurendeau, A.: Nonlinear site

460   response evidence of K-NET and KiK-net records from the 2011 off the Pacific

461   coast of Tohoku Earthquake. Earth, Planets and Space, 63(7), 785-789.

462   https://doi.org/10.5047/eps.2011.06.012, 2011.

463   Donner, S., Bernauer, M., and Igel, H.: Inversion for seismic moment tensors combining

464   translational and rotational ground motions, Geophys. J. Int., 207(1), 562-570,

465   https://doi.org/10.1093/gji/ggw298, 2016.

466   Feng, X., Fehler, M., Brown, S., Szabo, T. L., and Burns, D.: Short-period nonlinear

467   viscoelastic memory of rocks revealed by copropagating longitudinal acoustic

468   waves, J. Geophys. Res.-Solid Earth, 123(5), 3993–4006,

469   https://doi.org/10.1029/2017JB015012, 2018.

470   Frankel, A. D., Carver, D. L., and Williams, R. A.: Nonlinear and linear site response

471   and basin effects in Seattle for the M 6.8 Nisqually, Washington, earthquake. Bull.

472   Seismol. Soc. Am., 92(6), 2090-2109. https://doi.org/10.1785/0120000738, 2002.

473   Graizer, V. M.: Strong motion recordings and residual displacements: what are we

474   actually recording in strong motion seismology? Seismol. Res. Lett., 8(4), 635-

475   639, https://doi.org/10.1785/gssrl.81.4.635, 2010.

476   Graizer, V. M.: Inertial seismometry methods, Earth Physics, 27(1), 51-61, 1991.

477   Graves, R. W.: Simulating seismic wave propagation in 3D elastic media using

478   staggered-frid finite differences, Bull. Seismol. Soc. Am., 86(4), 1091-1106, 1996.

479   Gilbert, F.: Excitation of the normal modes of the Earth by earthquake sources, Geophys.

480   J. R. astr. Soc, 22(2), 223-226, https://doi.org/10.1111/j.1365-

481   246X.1971.tb03593.x, 1970.

482 Hua, S. B., and Zhang, Y.: Numerical experiments of moment tensor inversion with

483   rotational ground motions, Chinese J. Geophys., 65(1), 197-213,

484   https://doi.org/10.6038/cjg2022P0668, 2022 (in Chinese).

485 Huras, L., Zembaty, Z., Bonkowski, P. A., and Bobraet, P.: Quantifying local stiffness

486   loss in beams using rotation rate sensors, Mech. Syst. Signal Proc., 151, 107396,

487   https://doi.org/10.1016/j.ymssp.2020.107396, 2021.

488 Ichinose, G. A., Ford, S. R., and Mellors, R. J.: Regional moment tensor inversion using

489   rotational observations, J. Geophys. Res.-Solid Earth, 126(2), e2020JB020827,

490   https://doi.org/10.1029/2020JB020827, 2021.

491 Jost, M. L., and Hermann, R. B.: A students guide to and review of moment tensors,

492   Seism. Res. Lett., 60, 37-57, https://doi.org/10.1785/gssrl.60.2.37, 1989.

493 Knopoff, L., and Randall M. J.: The compensated linear-vector dipole: A possible

494   mechanism for deep earthquakes, J. Geophys. Res., 75(26), 4957–4963,

495   https://doi.org/10.1029/JB075i026p04957, 1970.

496 Kozak, J. T.: Tutorial on earthquake rotational effects: historical examples, Bull.

497   Seismol. Soc. Am., 99(2B), 998-1010, https://doi.org/10.1785/0120080308, 2009.

498 Laske, G., Masters, G., Ma, Z. T., and Pasyanos, M.: Update on CRUST1. 0-A 1-degree

499   global model of Earth's crust, EGU General Assembly 2013, 15, EGU2013-2658,

500   2013.

501 Lee, W. H. K., Igel, H., Todorovska, M. I., and Trifunac, M. D.: Recent advances in

502   rotational seismology, Seismol. Res. Lett., 80(3), 479–490,

503   https://doi.org/10.1785/gssrl.80.3.479, 2009.

504 Li, H. N.: Study on rotational components of ground motion, Journal of Shenyang

505   Architectural and Civil Engineering Institute, 7(1), 88-93, 1991 (in Chinese).

506 Li, H. N., and Sun, L. Y.: Rotational components of earthquake ground motions derived

507   from   surface   waves,   Earthq.   Eng.   Eng.   Vib.,   21(1),   15-23,

508   https://link.oversea.cnki.net/doi/10.13197/j.eeev.2001.01.003, 2001 (in Chinese).

509 Li, P. X., Lin, W. J., Zhang, X. M., Wang, X. M.: Comparisons for regular splitting

510   and non-splitting perfectly matched layer absorbing boundary conditions. Acta

511   Acustica, 40(01), 44-53, https://link.oversea.cnki.net/doi/10.15949/j.cnki.0371-

512   0025.2015.01.006, 2015.

513 Régnier, J., Bonilla, L. F., Bard, P. Y., et al.: PRENOLIN: International benchmark on

514   1D nonlinear site-response analysis—Validation phase exercise. Bul. Seismol.

515   Society of America, 108(2), 876-900. https://doi.org/10.1785/0120170210, 2018.

516 Renaud, G., Le Bas, P. Y., and Johnson, P. A.: Revealing highly complex elastic

517   nonlinear (anelastic) behavior of Earth materials applying a new probe: Dynamic

518   acoustoelastic   testing,   J.   Geophys.   Res.-Solid   Earth,   117,   B06202,

519   https://doi.org/10.1029/2011JB009127, 2012.

520 Renaud, G., Rivière, J., Le Bas, P. Y., and Johnson, P. A.: Hysteretic nonlinear elasticity

521   of Berea sandstone at low-vibrational strain revealed by dynamic acoustoelastic

522   testing, Geophys. Res. Lett., 40(4), 715-719, https://doi.org/10.1002/grl.50150,

523   2013.

524 Sun, L., Yu, Y., Lin, J. Q., and Liu, J. L.: Study on seismic rotation effect of simply

525   supported skew girder bridge, Earthquake Engineering and Engineering Dynamics,

526   37(4), 121-128, https://doi.org/10.13197/j.eeev.2017.04.121.sunl.014, 2017 (in

527   Chinese).

528   Sun, L. X., Zhang, Z., and Wang, Y.: Six-component elastic-wave simulation and

529   analysis, EGU General Assembly 2018, Geophysical Research Abstracts, 20,

530   EGU2018-14930-1, 2018.

531   TenCate, J. A., Malcolm, A. E., Feng, X., and Fehler, M. C.: The effect of crack

532   orientation on the nonlinear interaction of a P wave with an S wave, Geophys. Res.

533   Lett., 43(12), 6146-6152, https://doi.org/10.1002/2016GL069219, 2016.

534   Tromp, J., and Trampert, J.: Effects of induced stress on seismic forward modelling and

535   inversion. Geophys. J. Int., 213(2), 851-867. https://doi.org/10.1093/gji/ggy020,

536   2018.

537   Virieux, J.: P-SV wave propagation in heterogeneous media; velocity-stress finite-

538   difference method, Geophysics, 51(4), 889-901,

539   https://doi.org/10.1190/1.1442147, 1986.

540   Xu, Y. X., Xia, J. H., and Miller, R. D.: Numerical investigation of implementation of

541   airearth boundary by acoustic-elastic boundary approach, Geophysics, 72 (5),

542   SM147–SM153, https://doi.org/10.1190/1.2753831, 2007.

543   Yan, Y. Y.: Seismic response analysis of high-rise building under different types of

544   multi-dimensional earthquake ground motions (Ph.D. dissertation), Jiangsu

545   University, 2017(in Chinese).

546   Zhou, C., Zeng, X. Z., Wang, Q. L., Liu, W. Y., and Wang, C. Z.: Rotational motions of

547   the Ms7.0 Jiuzhaigou earthquake with ground tilt data, Science China Earth

548   Science, 62(5), 832-842, https://doi.org/10.1007/s11430-018-9320-3, 2019.